Article

Valley formation aridifies East Africa and elevates Congo Basin rainfall

https://doi.org/10.1038/s41586-022-05662-5

Received: 9 May 2022

Accepted: 9 December 2022

Published online: 01 March 2023

Check for updates

Callum Munday[1]✉, Nicholas Savage[2], Richard G. Jones[2] & Richard Washington[1]

East African aridification during the past 8 million years is frequently invoked as a driver of large-scale shifts in vegetation[1] and the evolution of new animal lineages, including hominins[2–4]. However, evidence for increasing aridity is debated[5] and, crucially, the mechanisms leading to dry conditions are unclear[6]. Here, numerical model experiments show that valleys punctuating the 6,000-km-long East African Rift System (EARS) are central to the development of dry conditions in East Africa. These valleys, including the Turkana Basin in Kenya, cause East Africa to dry by channelling water vapour towards Central Africa, a process that simultaneously enhances rainfall in the Congo Basin rainforest. Without the valleys, the uplift of the rift system leads to a wetter climate in East Africa and a drier climate in the Congo Basin. Results from climate model experiments demonstrate that the detailed tectonic development of Africa has shaped the rainfall distribution, with profound implications for the evolution of African plant and animal lineages.

East Africa is the driest equatorial landmass on the planet—an unexplained quirk in the classic Hadley model of tropical circulation[7]. Owing to the relatively low annual precipitation (mainly <800 mm year^{-1} in recent decades)[8] and propensity to drought[9], much of East Africa is unable to support dense forest. This is in contrast to the widespread rainforests of central and western equatorial Africa, where annual rainfall is higher, by 150–300% (ref. [10]). Over the past 8 million years, the reduction in East African dense forest, and associated expansion of mixed and grassland habitats[1], has been linked to the evolution of new animal lineages[1], including hominins[2–4]. There is no convincing climatic mechanism explaining this transition and which accounts for continued presence of dense forest in Central Africa. One hypothesis is that drier conditions in East Africa evolved with the uplift of the 6,000-km-long EARS[11,12]; however, mechanisms that relate uplift to rainfall deficits are problematic. In this paper, we demonstrate that the formation of valleys, rather than the uplift alone, is crucial to the low rainfall totals in East Africa. The valleys cause East Africa to dry by channelling water vapour towards Central Africa, a process that simultaneously favours rainfall in the Congo Basin rainforest. Without the valleys, the uplift of the EARS would lead to a wetter climate in East Africa and a drier climate in the Congo Basin.

The EARS separates relatively dry regions of Eastern Africa from wetter Central Africa. It is a leaky barrier to moisture-laden tropical easterly winds, which have been present from at least the Middle Miocene[13]. A series of fault-bounded valleys, oriented east to west, punctuate uplifted topographic domes along the EARS, including the Ethiopian and Kenyan highlands. The valleys are key conduits for water vapour transport from the Indian Ocean to Central Africa, with transport occurring by means of five main easterly low-level jets (LLJs), which accelerate as they are constrained by the valley sides[14,15] (Extended Data Fig. 1). Strong LLJs lead to enhanced water vapour export from East Africa, resulting in low rainfall[15–17]. The valleys—and associated water vapour pathways—probably reached their present-day morphology in the later stages of EARS development (after 10 million years ago (Ma) (ref. [18])). We hypothesize that they are central to the present-day rainfall distribution.

To test this hypothesis, we alter the valleys in a series of 20-year climate model experiments using a 25-km-resolution Pan-African regional climate model from the UK Met Office (see details of the model setup, evaluation and experiments in Methods). The model performs well in its simulation of present-day rainfall and circulation (Extended Data Figs. 1 and 2). Our initial focus is on the Turkana Channel, which is the largest of the fault-bounded valleys. The Turkana Jet—which forms in this valley—is responsible for a large portion of the easterly water vapour transport across the rift system[17]. Phases when the Turkana Jet is strong are associated with drought across the bimodal (two rainy seasons) region of East Africa[15–17] and increased rainfall in downstream regions, including the Ethiopian Highlands and parts of Central Africa[16,19]. We progressively alter the Turkana Channel from a blocked Turkana Channel (A), an incipient channel (B), the control (C; observed topography) and a deeper-than-observed channel (D) (Fig. 1).

The role of the Turkana Channel

Progressive drying occurs in East Africa with the deepening of the Turkana Channel, corresponding to experiments A–D (Fig. 2). Annual mean rainfall is highest in East Africa in the Turkana blocked experiment (Fig. 2a). In this experiment, the model simulates 1,000 mm year^{-1} (+500%) more rainfall in parts of dry northern Kenya and South Sudan compared with the control. Rainfall is lower across rainforest regions of central and western Central Africa, with a reduction of 300 mm year^{-1} near the Atlantic coast. As the channel deepens from experiments B to D, including the control, the upstream region of East Africa becomes progressively drier, whereas the Congo Basin becomes wetter. In the deeper-than-observed experiment (Fig. 2c),

[1]Climate Research Lab, School of Geography and the Environment, University of Oxford, Oxford, UK. [2]Met Office Hadley Centre, Exeter, UK. ✉e-mail: callum.munday@ouce.ox.ac.uk

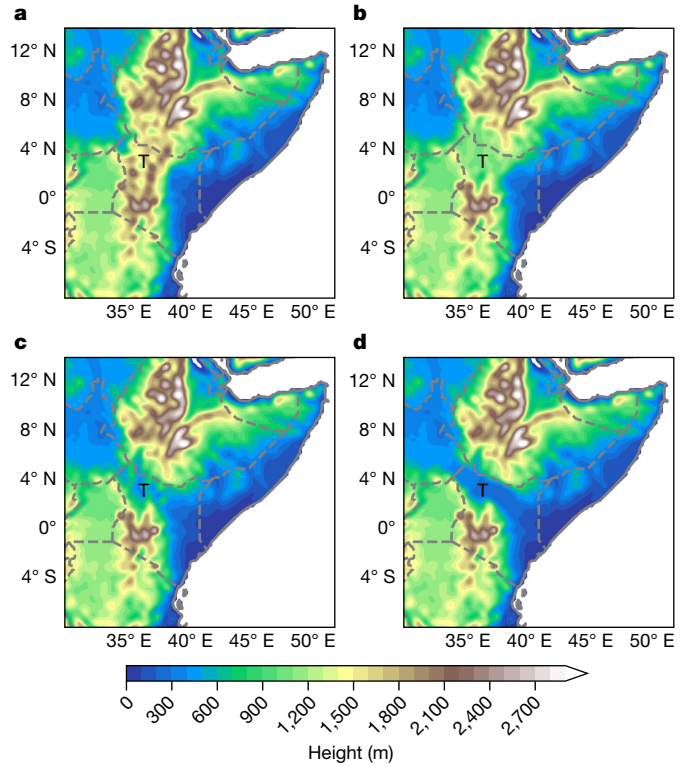

Fig. 1 | Overview of model experiments. Surface altitude (m) for the four Turkana experiments: blocked (**a**), incipient (**b**), control (**c**) and deeper-than-observed channel (**d**). The 'T' marks the location of the Turkana Channel.

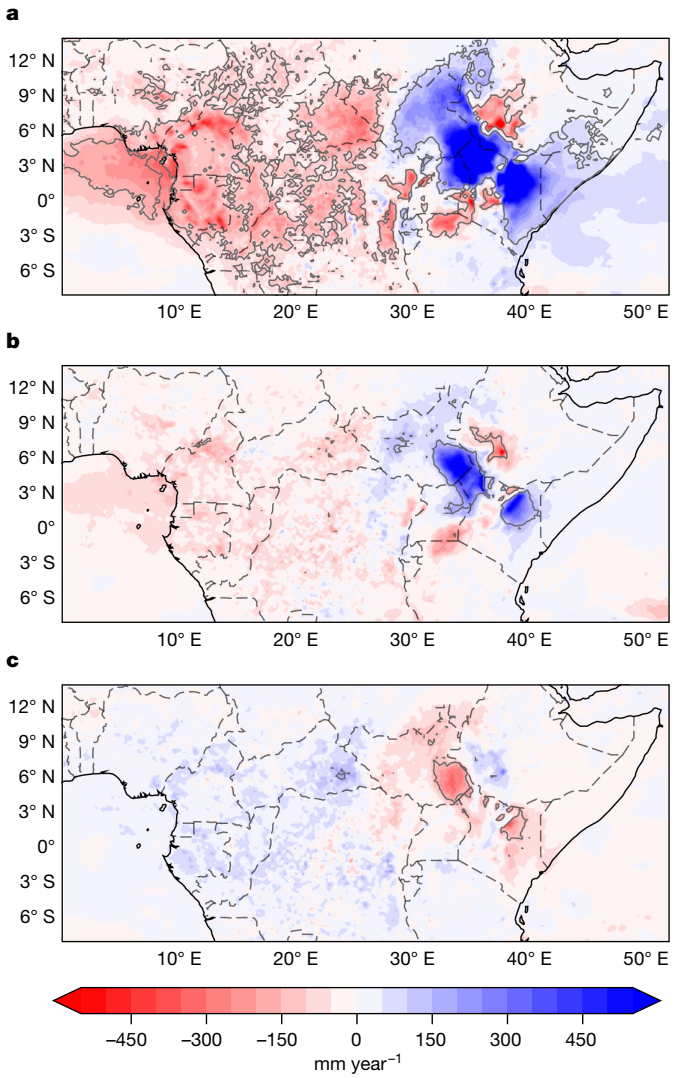

Fig. 2 | The Turkana Channel influences the east–west rainfall gradient in tropical Africa. Annual rainfall anomalies in the experiments compared with control (mm year^{-1}) for Turkana Channel blocked (**a**), incipient (**b**) and deeper-than-observed channel (**c**). Grey contours indicate regions with statistically significant differences between the control and the experiments based on the two-tailed Mann–Whitney *U* test, after controlling for the FDR, following Wilks[31] (see Methods). The P_{FDR} ($n = 20$) values are 0.024, 0.002 and 0.0008 for **a**,**b** and **c**, respectively.

rainfall is reduced in parts of East Africa and South Sudan by 200–400 mm year^{-1} (−30% to 50%). This demonstrates the contribution of the Turkana Channel to the east–west rainfall gradient: the presence of the channel reduces rainfall in East Africa and contributes to the high rainfall totals in Central Africa. The decrease in rainfall over East Africa induced by the Turkana Channel is consistent across all months.

Changes to the integrated water vapour transport (IWVT) help to diagnose the rainfall alterations (Fig. 3). In the blocked experiment (Fig. 3a), there is little easterly water vapour flux from East Africa to Central Africa north of the equator, as the Turkana LLJ is no longer present. IWVT anomalies in the blocked experiment are more than 100 kg m^{-1} s^{-1}. The weakened easterlies are still present in the incipient valley experiment (Fig. 3b). In the deeper-valley experiment (Fig. 3c), there is enhanced easterly water vapour export, associated with the reduced rainfall in East Africa compared with the control. Downstream of the valley in South Sudan, rainfall decreases in the deeper-valley experiment, as there is increased moisture divergence with a stronger jet. In the blocked experiment, rainfall increases in the South Sudan region.

Pan-African effect of valleys

The Turkana Jet is one of five main easterly LLJs that form across the EARS, the others forming in the Limpopo and Zambezi river valleys and across topographic lows in the Tanzanian and Malawi highlands[17,20,21]. These LLJs, and associated valleys, are important for water vapour export, and we posit that they have a similar effect on the east–west rainfall gradient.

To test this hypothesis, we carry out a further experiment (E, no valleys), which blocks all the main topographic lows across the EARS, from the Turkana Channel in the north to the Limpopo River valley in the south (Fig. 4). One can think of this experiment as imposing Andean-like topography across the eastern part of Africa. We find a Pan-African effect on the annual mean rainfall (Fig. 4). Rainfall increases across the entire eastern coastal sector of Africa and in the equatorial Indian Ocean, whereas there is large-scale drying in the continental interior and particularly along the western coast and in South Africa.

In the 'no valleys' experiment, the large-scale wetting is associated with a reduction in water vapour flux through the main valleys (Fig. 4c,d). Meanwhile, in the control experiment, the valleys in the rift system export water vapour from East Africa. The total IWVT across the rift system (see Methods) in the 'no valleys' experiment (2.14×10^8 kg s^{-1}) is 25% less than in the control (2.82×10^8 kg s^{-1}). This leaves more water vapour available for rainfall across Eastern Africa in the 'no valleys' experiment (3.66×10^7 kg s^{-1}) compared with the control simulation (2.73×10^7 kg s^{-1}) (see Methods for moisture budget calculation).

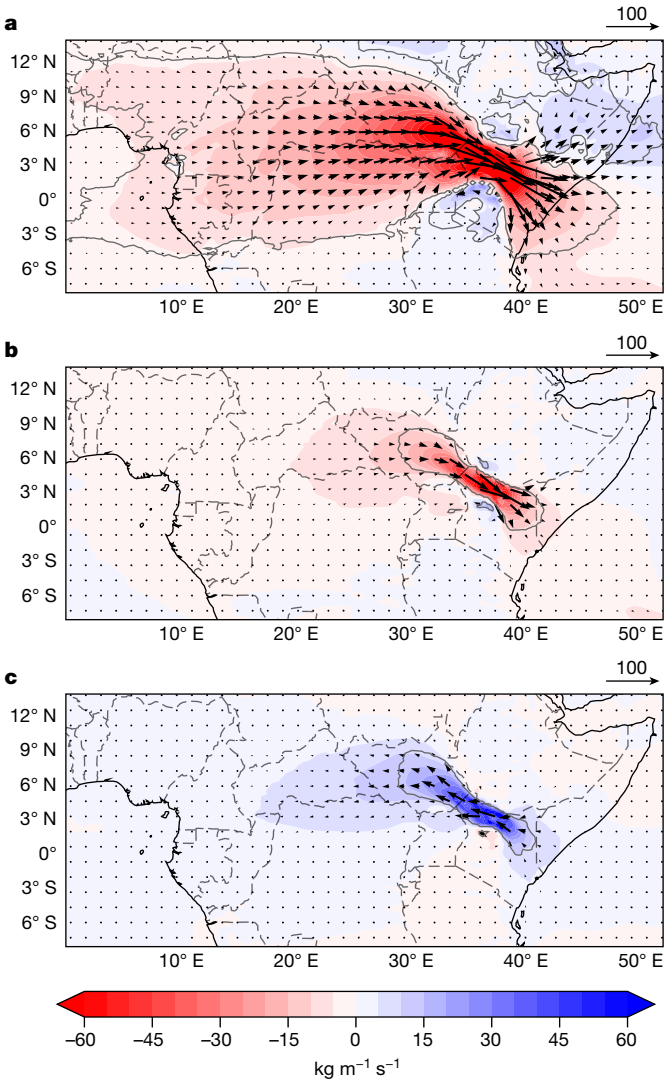

Fig. 3 | Water vapour export from East Africa increases as the Turkana Channel deepens. IWVT anomalies (kg m^{-1} s^{-1}; shading) and vectors compared with control (annual mean) for the three Turkana experiments compared with control: Turkana Channel blocked (**a**), incipient (**b**) and deeper-than-observed channel (**c**). Grey contours indicate regions with statistically significant differences (evaluated on the IWVT field) calculated by means of the two-tailed Mann–Whitney *U* test, after controlling for the FDR, following Wilks[31] (see Methods). The P_{FDR} values ($n = 20$) are 0.032, 0.001 and 0.001 for **a**, **b** and **c**, respectively.

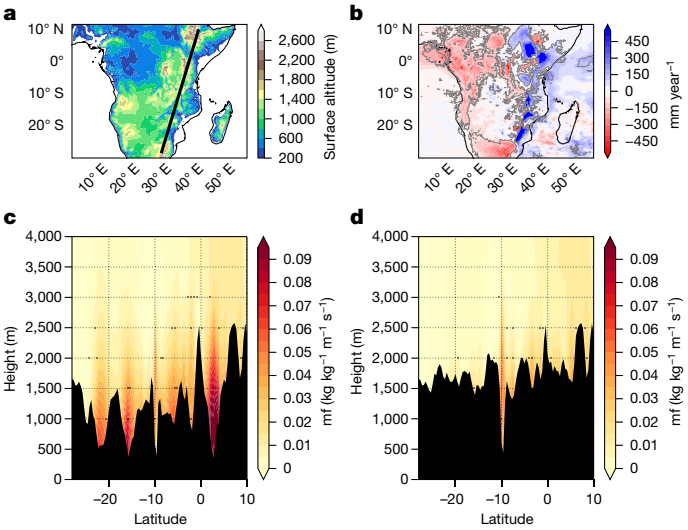

Fig. 4 | Valleys lead to lower rainfall in East Africa, with increased water vapour export across the rift system. a, Surface altitude (m) for the control simulation. **b**, The rainfall anomaly (no valleys − control; mm $year^{-1}$). Vertical cross-sections of the water vapour flux (moisture flux, mf; kg kg^{-1} m^{-1} s^{-1}) perpendicular to the black line shown in **a** (positive easterly, negative westerly) for the control (**c**) and 'no valleys' (**d**) experiments. The black filled area indicates the surface height in each experiment. The grey contours in **b** indicate statistically significant differences in rainfall, calculated by means of the two-tailed Mann–Whitney *U* test, after controlling for the FDR, following Wilks[31] (see Methods). The P_{FDR} value ($n = 20$) is 0.022.

Discussion

The presence of valleys within the EARS leads to a drier East Africa and wetter Congo Basin. Previous modelling studies have implicated the rift system in East African dryness[12,22–24], but the shared assumption in these studies is that the uplift alone—which mainly occurred before 10 Ma—causes the aridity. In the 'no valleys' experiment, we show mechanistically that uplift alone does the opposite: the removal of valleys reduces the water vapour export from East Africa, whereas the regions of high topography act as an elevated heat source. This favours convection in East Africa, while necessarily reducing convection in the Congo rainforest, as diagnosed by the reduction in water vapour transport across the rift system. Another important factor in East African aridity, the Somali Jet, strengthens in response to an uninterrupted barrier in the blocked valley experiments (Fig. 3). This is consistent with other modelling studies, which show a weakening of the Somali Jet when the rift system is lowered[22,24].

The expansion of grassland and mixed habitats, at the expense of dense forest, across East Africa in the past 8 million years is linked with broad faunal turnover[1] and is a cornerstone for several hypotheses relating to hominid evolution[2,4,25–28]. The lower rainfall in East Africa owing to the formation of valleys is capable of explaining the large-scale vegetation shift. Although estimates for the timing of valley formation vary between studies and across the EARS, processes occurring in the past 10 Ma have shaped the present-day morphology[11,18]. Other global climate events could have contributed to the expansion of grasslands, including the late Miocene cooling (5–7 Ma)[29] and onset of Northern Hemisphere glaciation (about 2.75 Ma)[30], but the development of valleys is an obvious proximate driver for rainfall change. Today, the presence of valleys is a key explanation for why East Africa is curiously dry for its latitude and prone to drought.

Online content

Any methods, additional references, Nature Portfolio reporting summaries, source data, extended data, supplementary information, acknowledgements, peer review information; details of author contributions and competing interests; and statements of data and code availability are available at https://doi.org/10.1038/s41586-022-05662-5.

1. Bobe, R. The evolution of arid ecosystems in eastern Africa. *J. Arid. Environ.* **66**, 564–584 (2006).
2. deMenocal, P. B. African climate change and faunal evolution during the Pliocene–Pleistocene. *Earth Planet. Sci. Lett.* **220**, 3–24 (2004).
3. Maslin, M. A., Shultz, S. & Trauth, M. H. A synthesis of the theories and concepts of early human evolution. *Philos. Trans. R. Soc. B Biol. Sci.* **370**, 20140064 (2015).
4. Vrba, E. S. in *Evolutionary History of the "Robust" Australopithecines* (ed. Grine, F. E.) 405–426 (Aldine de Gruyter, 1988).
5. Blumenthal, S. A. et al. Aridity and hominin environments. *Proc. Natl Acad. Sci. USA* **114**, 7331–7336 (2017).
6. Levin, N. E. Environment and climate of early human evolution. *Annu. Rev. Earth Planet. Sci.* **43**, 405–429 (2015).
7. Trewartha, G. T. *The Earth's Problem Climates* (Univ. Wisconsin Press, 1961).
8. Yang, W., Seager, R., Cane, M. A. & Lyon, B. The annual cycle of East African precipitation. *J. Clim.* **28**, 2385–2404 (2015).

9. Nicholson, S. E. Climate and climatic variability of rainfall over eastern Africa. *Rev. Geophys.* **55**, 590–635 (2017).
10. Washington, R., James, R., Pearce, H., Pokam, W. M. & Moufouma-Okia, W. Congo Basin rainfall climatology: can we believe the climate models? *Philos. Trans. R. Soc. B Biol. Sci.* **368**, 20120296 (2013).
11. Ring, U. The East African rift system. *Austrian J. Earth Sci.* **107**, 132–146 (2014).
12. Sepulchre, P. et al. Tectonic uplift and Eastern Africa aridification. *Science* **313**, 1419–1423 (2006).
13. Betzler, C. et al. The abrupt onset of the modern South Asian Monsoon winds. *Sci. Rep.* **6**, 29838 (2016).
14. Indeje, M., Semazzi, F. H. M., Xie, L. & Ogallo, L. J. Mechanistic model simulations of the East African climate using NCAR regional climate model: influence of large-scale orography on the Turkana low-level jet. *J. Clim.* **14**, 2710–2724 (2001).
15. Nicholson, S. The Turkana low-level jet: mean climatology and association with regional aridity. *Int. J. Climatol.* **36**, 2598–2614 (2016).
16. Vizy, E. K. & Cook, K. H. Observed relationship between the Turkana low-level jet and boreal summer convection. *Clim. Dyn.* **53**, 4037–4058 (2019).
17. Munday, C., Washington, R. & Har, N. African low-level jets and their importance for water vapor transport and rainfall. *Geophys. Res. Lett.* **48**, e2020GL090999 (2021).
18. Chorowicz, J. The East African rift system. *J. Afr. Earth Sci.* **43**, 379–410 (2005).
19. Viste, E. & Sorteberg, A. Moisture transport into the Ethiopian highlands. *Int. J. Climatol.* **33**, 249–263 (2013).
20. Spavins-Hicks, Z. D., Washington, R. & Munday, C. The Limpopo Low-Level Jet: mean climatology and role in water vapor transport. *J. Geophys. Res. Atmos.* **126**, e2020JD034364 (2021).
21. Barimalala, R., Blamey, R. C., Desbiolles, F. & Reason, C. J. C. The influence of southeastern African river valley jets on regional rainfall. *Clim. Dyn.* **57**, 2905–2920 (2021).
22. Slingo, J., Spencer, H., Hoskins, B., Berrisford, P. & Black, E. The meteorology of the Western Indian Ocean, and the influence of the East African Highlands. *Philos. Trans. R. Soc. A Math. Phys. Eng. Sci.* **363**, 25–42 (2005).
23. Prömmel, K., Cubasch, U. & Kaspar, F. A regional climate model study of the impact of tectonic and orbital forcing on African precipitation and vegetation. *Palaeogeogr. Palaeoclimatol. Palaeoecol.* **369**, 154–162 (2013).
24. Jung, G., Prange, M. & Schulz, M. Influence of topography on tropical African vegetation coverage. *Clim. Dyn.* **46**, 2535–2549 (2016).
25. DeMenocal, P. B. Plio-Pleistocene African climate. *Science* **270**, 53–59 (1995).
26. Cerling, T. E. et al. Woody cover and hominin environments in the past 6 million years. *Nature* **476**, 51–56 (2011).
27. Maslin, M. A. et al. East African climate pulses and early human evolution. *Quat. Sci. Rev.* **101**, 1–17 (2014).
28. Trauth, M. H. et al. Northern Hemisphere Glaciation, African climate and human evolution. *Quat. Sci. Rev.* **268**, 107095 (2021).
29. Herbert, T. D. et al. Late Miocene global cooling and the rise of modern ecosystems. *Nat. Geosci.* **9**, 843–847 (2016).
30. Hodell, D. A. & Channell, J. E. T. Mode transitions in Northern Hemisphere glaciation: co-evolution of millennial and orbital variability in Quaternary climate. *Clim. Past* **12**, 1805–1828 (2016).
31. Wilks, D. The stippling shows statistically significant grid points. *Bull. Am. Meteorol. Soc.* **97**, 2263–2274 (2016).

Methods

The model

The model used is the UK Met Office Unified Model set up in the GA7.05 configuration[32]. The model run is from 1990 to 2009 at a 25-km horizontal resolution over a Pan-African domain (34.5° S to 25° N, 13° W to 73° E). The model has a non-hydrostatic semi-implicit and semi-Lagrangian dynamical core[33] and uses a mass-flux convection scheme based on Gregory and Rowntree[34]. Lateral atmospheric boundary conditions are provided by six-hourly fields of temperature, humidity, winds and surface pressure[35] from ERA-Interim reanalysis[36] and daily sea-surface temperatures are prescribed on the basis of the NOAA Daily OISST v2.1 daily reanalysis[37].

To establish the adequacy of the control run, we compare the model data with observed and reanalysis datasets. For precipitation, we compare climatological rainfall with Climate Hazards Group InfraRed Precipitation with Station data (CHIRPS) precipitation[38] and Global Precipitation Climatology Project (GPCP) version 2.2 (ref. [39]) (Extended Data Fig. 1). The control run captures the observed distribution of rainfall over Africa, with rainfall hotspots over Madagascar, the Ethiopian Highlands, the Kenyan Highlands, the Rwenzori Mountains and the Cameroonian Highlands. Compared with CHIRPS, the model overestimates rainfall in some of these regions, including in parts of Central Africa and the Ethiopian Highlands. The overestimation of rainfall in the Congo Basin is a common issue across climate models (such as refs. [40,41]). The model performs excellently in East Africa, successfully simulating the low annual rainfall totals.

We compare the model circulation with the latest European Centre for Medium-Range Weather Forecasts (ECMWF) reanalysis product (ERA5)[42]. We focus our attention on the zonal and meridional vertically integrated water vapour transport, which is a key diagnostic in Fig. 3. These are calculated on model levels using specific humidity (q) and zonal (u) and meridional (v) winds, as:

$$Qu = \int_{\text{surface}}^{\text{toa}} qu \frac{\mathrm{d}P}{g}$$

$$Qv = \int_{\text{surface}}^{\text{toa}} qv \frac{\mathrm{d}P}{g}$$

$$\text{IWVT} = \sqrt{Qu^2 + Qv^2}$$

in which P is pressure and g is gravitational acceleration (9.81 m s^{-2}), and IWVT is the integrated water vapour transport (kg m^{-1} s^{-1}). The model performs very well in simulating the integrated water vapour flux in comparison with the ERA5 reanalysis (Extended Data Fig. 2). In particular, the model is able to capture the magnitude and distribution of easterly valley jets along the EARS (including the Turkana Jet at about 3° N, 36° E), as well as the southeasterly and southwesterly components of the Somali Jet in the western Indian Ocean.

The experiments

Figure 1 shows the topography in experiments A–D and Fig. 4d shows the topography cross-section in experiment E. For each experiment, we manually edited the valleys in the high-resolution topography file (1-km resolution; NOAA GLOBE digital elevation model[43]) using the open-source GIMP editing software. We altered the high-resolution topography file to address both resolved and sub-grid-scale orographic influences (for example, orographic drag), which are parameterized in the model. The altered high-resolution orography field was used to create new ancillary files (boundary conditions) for each experiment.

The experiments differ from other approaches to understanding orographic effects, which apply a scaling factor to the overall orographic field, for example, by progressively reducing the height of the topography by a given percentage. The approach used here allows us to isolate the effect of the specific geomorphology of interest: the valleys. Because the aim of the experiments is to isolate the effect of valleys on African climate, we do not purport to reproduce specific timespans of Earth's history. The latter is made difficult by a paucity of data on conditions at the time and a lack of agreement between studies on the actual evolution of African topography over the Miocene–Pliocene period[11]. The sensitivity of African climate to valleys, shown in our experiments, suggests that, to clarify temporally linked orographic and climate dynamics, data need to be collected at a sufficient resolution to allow timescales of valley development to be distinguished from broader-scale uplift rates.

Moisture budget calculation

We calculate the moisture budget for the East African region upstream of the rift system shown in Extended Data Fig. 1. On the basis of the Qu and Qv components of the integrated moisture flux, we first use the MetPy cross_section_components function (https://unidata.github.io/MetPy/latest/api/generated/metpy.calc.cross_section_components.html) to find the component of the IWVT normal (inflow) to each segment of the regional boundary (Q_n). We then integrate across each segment separately to find the total segment contribution:

$$Q_{\text{seg}} = \int_{l_0}^{l_n} Q_\text{n} \mathrm{d}l$$

in which l is the length of the segment (m) and dl is about 26,000 m (corresponding to the average grid length for the model). We define positive contributions as moisture entering the region and negative contributions as moisture leaving the region. Finally, we sum the contributions from all segments to calculate the moisture budget.

Statistical testing

The two-tailed Mann–Whitney U test is used to evaluate a null hypothesis of no difference between the experiments and the control (n = 20 years). We follow Wilks[31] in applying a constraint on the false discovery rate (FDR) based on the distribution of P-values from each grid point in the composite map. The false discovery control level (α_{FDR}) is set conservatively following Wilks[31] as $2\alpha_{\text{global}}$, in which $\alpha_{\text{global}} = 0.05$, such that $\alpha_{\text{FDR}} = 0.10$. We report the threshold P_{FDR} for each test in the relevant figure captions.

Data availability

Model data arising from this paper used in plotting and the edited high-resolution GLOBE dataset orography files for each experiment are available on publication at https://doi.org/10.5281/zenodo.6956995. ERA5 data were downloaded from https://cds.climate.copernicus.eu/cdsapp#!/home. CHIRPS data are available at https://data.chc.ucsb.edu/products/CHIRPS-2.0/. GPCP data are from https://www.ncei.noaa.gov/access/metadata/landing-page/bin/iso?id=gov.noaa.ncdc:C00979. Data used in base maps for figures are publicly available from https://www.naturalearthdata.com/ and plotted with Cartopy (https://github.com/SciTools/cartopy/archive/v0.11.2.tar.gz). The UK Met Office Unified Model is available for use under license. For further information on how to apply for a license, see http://www.metoffice.gov.uk/research/modelling-systems/unified-model.

Code availability

Code for producing figures is available on publication at https://doi.org/10.5281/zenodo.6956995.

32. Tucker, S. O. et al. Evaluation of a new 12 km regional perturbed parameter ensemble over Europe. *Clim. Dyn.* **58**, 879–903 (2022).
33. Wood, N. et al. An inherently mass-conserving semi-implicit semi-Lagrangian discretization of the deep-atmosphere global non-hydrostatic equations. *Q. J. R. Meteorol. Soc.* **140**, 1505–1520 (2014).
34. Gregory, D. & Rowntree, P. R. A mass flux convection scheme with representation of cloud ensemble characteristics and stability-dependent closure. *Mon. Weather Rev.* **118**, 1483–1506 (1990).
35. Davies, T. Lateral boundary conditions for limited area models. *Q. J. R. Meteorol. Soc.* **140**, 185–196 (2014).
36. Dee, D. P. et al. The ERA-Interim reanalysis: configuration and performance of the data assimilation system. *Q. J. R. Meteorol. Soc.* **137**, 553–597 (2011).
37. Reynolds, R. W. et al. Daily high-resolution-blended analyses for sea surface temperature. *J. Clim.* **20**, 5473–5496 (2007).
38. Funk, C. et al. The climate hazards infrared precipitation with stations—a new environmental record for monitoring extremes. *Sci. Data* **2**, 150066 (2015).
39. Adler, R. F. et al. The Global Precipitation Climatology Project (GPCP) monthly analysis (new version 2.3) and a review of 2017 global precipitation. *Atmosphere* **9**, 138 (2018).
40. Creese, A. & Washington, R. Using qflux to constrain modeled Congo Basin rainfall in the CMIP5 ensemble. *J. Geophys. Res. Atmos.* **121**, 13,415–13,442 (2016).
41. Haensler, A., Saeed, F. & Jacob, D. Assessing the robustness of projected precipitation changes over central Africa on the basis of a multitude of global and regional climate projections. *Clim. Change* **121**, 349–363 (2013).
42. Hersbach, H. et al. The ERA5 global reanalysis. *Q. J. R. Meteorol. Soc.* **146**, 1999–2049 (2020).
43. Hastings, D. A. et al. *The Global Land One-kilometer Base Elevation (GLOBE) Digital Elevation Model, Version 1.0* (National Oceanic and Atmospheric Administration, 1999); http://www.ngdc.noaa.gov/mgg/topo/globe.html.

Acknowledgements We acknowledge the input from and useful discussions with J. Lee-Thorp and R. Bobé (both Oxford University). This article is an output from the REACH programme, financed by UK Aid from the UK Foreign, Commonwealth and Development Office (FCDO) for the benefit of developing countries (programme code 201880). However, the views expressed and information contained in it are not necessarily those of or endorsed by the FCDO, which can accept no responsibility for such views or information or for any reliance placed on them.

Author contributions C.M. designed and ran the model experiments and wrote the manuscript. N.S. helped set up and run the model experiments and wrote part of the Methods section. R.W. contributed to the design of the experiments and edited the manuscript. R.G.J. contributed to the experimental design and edited the manuscript.

Competing interests The authors declare no competing interests.

Additional information

Correspondence and requests for materials should be addressed to Callum Munday.

Peer review information *Nature* thanks Thierry C. Fotso-Nguemo and the other, anonymous, reviewer(s) for their contribution to the peer review of this work.

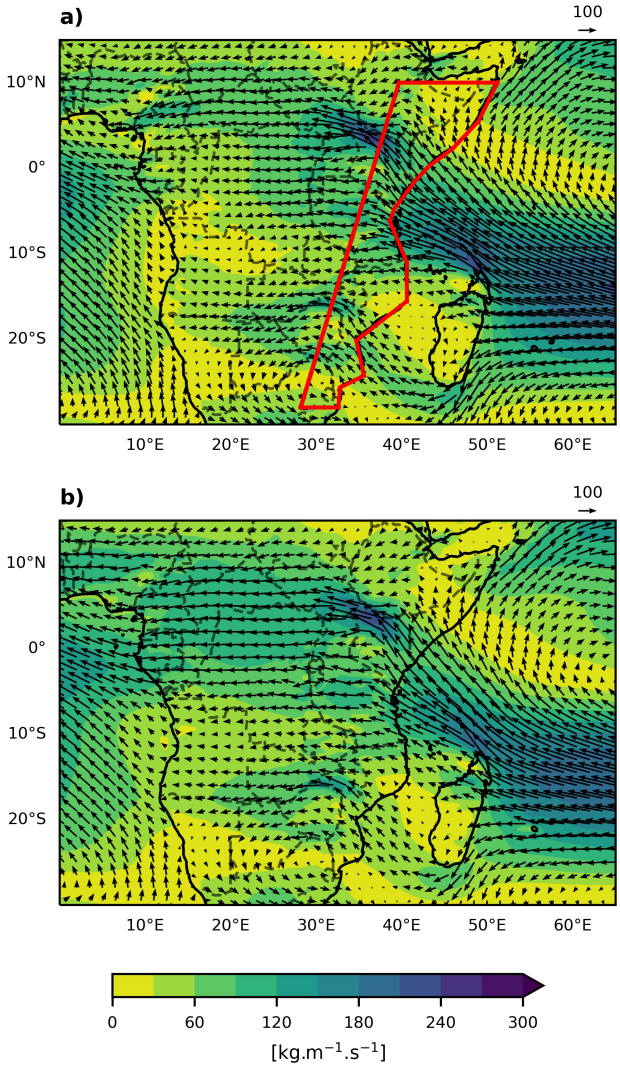

Extended Data Fig. 1 | Water vapour transport in control and reanalysis data. The arrows show the direction and strength at which atmospheric-column integrated water vapour is being transported (kg m^{-1} s^{-1}) in the control experiment (**a**) and ERA5 (**b**). Shading gives the IWVT magnitude (kg m^{-1} s^{-1}) (see Methods). The East African region we use to evaluate the moisture budget is bounded by the red line in **a**. ERA5 data[42] are available at https://cds.climate.copernicus.eu/cdsapp#!/home.

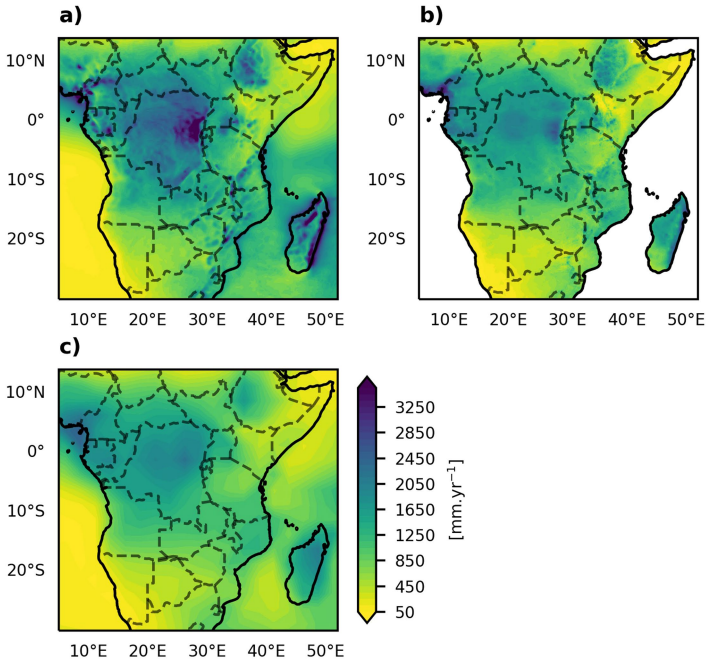

Extended Data Fig. 2 | Evaluation of rainfall in the control simulation. Annual rainfall (mm year^{-1}) in the control (**a**), CHIRPS (**b**) and GPCP version 2.2 (**c**). CHIRPS[38] data are available at https://data.chc.ucsb.edu/products/CHIRPS-2.0/. GPCP data[39] are from https://www.ncei.noaa.gov/access/metadata/landing-page/bin/iso?id=gov.noaa.ncdc:C00979.